

# Adaptive Galerkin Particle Method

Hongsheng Lu, Jiun-Shyan Chen

*Department of Civil & Environmental Engineering  
University of California, Los Angeles  
5731G Boelter Hall  
Los Angeles, CA 90095-1593*

## **Abstract**

*Adaptive procedures of a Galerkin particle method are presented. In the Galerkin particle method, the construction of shape functions and domain integration of weak form are entirely particle based. The stabilized conforming nodal integration is employed in the domain integration of weak form. The Voronoi diagram used as the nodal representative domain in the stabilization of nodal integration is employed as the hierarchy for adaptive refinement. Recovery based error indicator is introduced in the adaptive analysis. Owing to the smooth shape functions in Galerkin particle method, the stress recovery error indicator does not require any projection as was needed in the  $C^0$  finite element methods.*

## **1. Introduction**

In recent years, a new class of numerical methods, collectively called the meshfree method, has been developed as a generalization of finite element methods for computational mechanics [1-10]. Meshfree methods employ new approximation theories, such as moving least-squares [11] and reproducing kernel approximation [4] that allow the construction of shape functions without the need of an explicit mesh. These shape functions are naturally conforming and thus are ideal for adaptive computation.

An issue to be addressed in meshfree adaptivity is the domain integration. Gauss integration is commonly used in meshfree methods for integration of weak form. Due to the complexity involved in Gauss integration for meshfree methods, attempts have been made to develop nodal integration methods for meshfree computation [12-18]. Meshfree method with stabilized conforming nodal integration [18], herein referred to as a Galerkin particle method, offers a convenient hierarchical structure for adaptive refinement in meshfree analysis. In the stabilized conforming nodal integration, a strain smoothing stabilization was introduced as a means to meet integration constraints and to provide a stabilization for nodal integration. The strain smoothing is performed in the nodal representative domain generated by the Voronoi diagram. Using the properties of Voronoi diagram, Voronoi cells can be conveniently used as the reference for inserting nodes uniformly into the existing randomly distributed particles. The support sizes of the shape functions in the adaptive refinement can be determined using the geometry of Voronoi cells. Further, Voronoi cells also provide neighboring particle information for constructing the data structure in adaptivity analysis.

Recovery based error indicator is employed in the present work [19, 20]. Since the meshfree shape functions can be arbitrarily smooth, the stress recovery approach in the error indicator can

be formulated without projection procedures employed in the finite elements due to the  $C^0$  approximation of displacements.

This paper is arranged as follows. Section 2 reviews reproducing kernel approximation and the stabilized conforming nodal integration for Galerkin particle method. The implementation of adaptive method under the framework of Galerkin particle method is introduced in Section 3. Two numerical tests are presented in Section 4 to examine the effectiveness of the proposed method, and conclusions are given in Section 5.

## 2. Galerkin Particle Method

### 2.1 Shape Function

We start with a moving least-square or reproducing kernel approximation of a variable  $u(\mathbf{x})$ , denoted by  $u^h(\mathbf{x})$ , as

$$u^h(\mathbf{x}) = \sum_{l=1}^{NP} C(\mathbf{x}; \mathbf{x} - \mathbf{x}_l) \Phi_{a_l}(\mathbf{x} - \mathbf{x}_l) u_l \quad (2.1)$$

where  $\Phi_a(\mathbf{x} - \mathbf{x}_l)$  is a kernel function with compact support “ $a_l$ ”,  $u_l$  are the coefficients of approximation,  $NP$  is the number of particles,  $\Psi_l(\mathbf{x})$  is the meshfree shape function, and  $C(\mathbf{x}; \mathbf{x} - \mathbf{x}_l)$  is the correction function that introduces reproducibility of n-th order polynomial:

$$C(\mathbf{x}; \mathbf{x} - \mathbf{x}_l) = \sum_{p+q+r=0}^n (x_1 - x_{1l})^p (x_2 - x_{2l})^q (x_3 - x_{3l})^r b_{pqr}(\mathbf{x}) \equiv \mathbf{H}^T(\mathbf{x} - \mathbf{x}_l) \mathbf{b}(\mathbf{x}) \quad (2.2)$$

$$\mathbf{H}^T(\mathbf{x} - \mathbf{x}_l) = \{1, x_1 - x_{1l}, x_2 - x_{2l}, \dots, (x_3 - x_{3l})^n\} \quad (2.3)$$

By requiring exact representation of n-th order polynomial,  $\mathbf{b}(\mathbf{x})$  in Eq. (2.2) is solved and the shape function is obtained

$$\Psi_l(\mathbf{x}) = \mathbf{H}^T(\boldsymbol{\theta}) \mathbf{M}^{-1}(\mathbf{x}) \mathbf{H}(\mathbf{x} - \mathbf{x}_l) \Phi_a(\mathbf{x} - \mathbf{x}_l) \quad (2.4)$$

$$\mathbf{M}(\mathbf{x}) = \sum_{l=1}^{NP} \mathbf{H}(\mathbf{x} - \mathbf{x}_l) \mathbf{H}^T(\mathbf{x} - \mathbf{x}_l) \Phi_a(\mathbf{x} - \mathbf{x}_l) \quad (2.5)$$

### 2.2 Stabilized Galerkin Particle Method

For illustration, consider the following linear elasticity model problem:

$$\nabla \cdot \boldsymbol{\sigma} = \mathbf{b} \quad \text{in} \quad \Omega \quad (2.6)$$

$$\mathbf{u} = \mathbf{g} \quad \text{on} \quad \Gamma^g \quad (2.7)$$

$$\mathbf{n} \cdot \boldsymbol{\sigma} = \mathbf{h} \quad \text{on} \quad \Gamma^h \quad (2.8)$$

$$\boldsymbol{\sigma} = \mathbf{C} : \boldsymbol{\varepsilon} \quad (2.9)$$

$$\boldsymbol{\varepsilon} = \frac{1}{2} [(\nabla \mathbf{u}) + (\mathbf{u} \nabla)^T] \equiv \nabla^s \mathbf{u} \quad (2.10)$$

where  $\Omega$  is the problem domain,  $\Gamma^g$  and  $\Gamma^h$  are the Dirichlet and Neumann boundaries, respectively. If the approximation of  $\mathbf{u}$  is kinematically admissible, the Galerkin approximation of the above problem can be expressed as

$$\int_{\Omega} \delta \boldsymbol{\varepsilon}^h : \mathbf{C} : \boldsymbol{\varepsilon}^h d\Omega - \int_{\Omega} \delta \mathbf{u}^h \cdot \mathbf{f} d\Omega - \int_{\Gamma^h} \delta \mathbf{u}^h \cdot \mathbf{h} d\Gamma = 0 \quad (2.11)$$

$$\boldsymbol{\varepsilon}^h = \nabla^s \mathbf{u}^h = \sum_I \mathbf{B}_I \mathbf{u}_I \quad (2.12)$$

where  $\mathbf{B}_I$  is the gradient matrix associated with  $\nabla^s \mathbf{u}^h$ . Gauss integration is commonly used in Eq. (2.11) in Galerkin based meshfree methods. Issues associated with Gauss integration [17, 21] are (1) a specialized integration zone pattern is required, (2) Gauss integration fails to satisfy linear exactness in the Galerkin approximation, and (3) high computational cost. A direct nodal integration of Eq. (2.11), on the other hand, leads to a rank deficiency and numerical instability.

Linear exactness in Galerkin approximation of this model problem first requires at least linear basis be employed in the shape function for  $\mathbf{u}^h$  in Eq. (2.3). Second, numerical integration of stiffness and force must meet the following condition for interior nodes:

$$\int_{\Omega} \nabla \Psi_I(\mathbf{x}) d\Omega = \int_{\Gamma^h} \Psi_I(\mathbf{x}) \mathbf{n} d\Gamma \quad (2.13)$$

where  $\mathbf{n}$  is the surface normal on  $\Gamma^h$ . Equation (2.13) is called the integration constrain.

A stabilized conforming nodal integration (SCNI) method has been proposed [17] to: (1) provide stability to nodal integration, and (2) meet the integration constraints in Eq. (2.13). It starts with a smoothing of  $\nabla \mathbf{u}^h$  at the nodal representative domain by

$$\tilde{\nabla} u_i^h(\mathbf{x}_L) = \frac{1}{A_L} \int_{\Omega_L} \nabla u_i^h d\Omega; \quad A_L = \int_{\Omega_L} d\Omega \quad (2.14)$$

where  $\Omega_L$  is a nodal representative domain as shown in Fig. 2.1, and  $\tilde{\nabla}$  is the smoothed gradient operator.

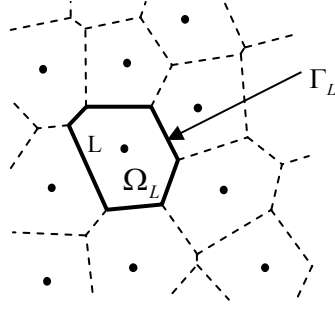


Figure 2.1 Nodal representative domain

The integration constraints can be accomplished by applying divergence theorem to Eq. (2.14) to yield

$$\tilde{\nabla} u_i^h(\mathbf{x}_L) = \frac{1}{A_L} \int_{\Gamma_L} \mathbf{n} u_i^h d\Gamma \quad (2.15)$$

where  $\Gamma_L$  is the boundary of the representative domain of node  $L$  as shown in Fig. 2.1. Introducing reproducing kernel shape functions into Eq. (2.15) yields

$$\tilde{\nabla} u_i^h(\mathbf{x}_L) = \sum_I \tilde{\nabla} \Psi_I(\mathbf{x}_L) u_{iI} \quad (2.16)$$

where

$$\tilde{\nabla} \Psi_I(\mathbf{x}_L) = \frac{1}{A_L} \int_{\Omega_L} \nabla \Psi_I(\mathbf{x}) d\Omega = \frac{1}{A_L} \int_{\Gamma_L} \Psi_I(\mathbf{x}) \mathbf{n}(\mathbf{x}) d\Gamma \quad (2.17)$$

Here  $\tilde{\nabla} \Psi_I(\mathbf{x}_L)$  is the smoothed  $\nabla \Psi_I(\mathbf{x})$  evaluated at point  $\mathbf{x}_L$ . It has been easily shown that this smoothed shape function gradient  $\tilde{\nabla} \Psi_I(\mathbf{x}_L)$  meets the integration constraint for nodal integration with weight  $A_L$ .

Following Eqns. (2.14)-(2.17), a smoothed strain can be defined as

$$\tilde{\boldsymbol{\varepsilon}}^h(\mathbf{x}_L) = \frac{1}{A_L} \int_{\Omega_L} \nabla^s \mathbf{u} d\Omega \equiv \sum_I \tilde{\mathbf{B}}_I \mathbf{u}_I \quad (2.18)$$

$$\tilde{\mathbf{B}}_I(\mathbf{x}_L) = \begin{bmatrix} \tilde{b}_{11}(\mathbf{x}_L) & 0 \\ 0 & \tilde{b}_{12}(\mathbf{x}_L) \\ \tilde{b}_{12}(\mathbf{x}_L) & \tilde{b}_{11}(\mathbf{x}_L) \end{bmatrix} \quad (2.19)$$

$$\tilde{b}_{li}(\mathbf{x}_L) = \frac{1}{A_L} \int_{\Gamma_L} \Psi_l(\mathbf{x}) n_i(\mathbf{x}) d\Gamma \quad (2.20)$$

Finally, a modified variational equation using an assumed strain method is introduced

$$\int_{\Omega} \delta \tilde{\boldsymbol{\varepsilon}}^h : \mathbf{C} : \tilde{\boldsymbol{\varepsilon}}^h d\Omega - \int_{\Omega} \delta \mathbf{u}^h \cdot \mathbf{b} d\Omega - \int_{\Gamma^h} \delta \mathbf{u}^h \cdot \mathbf{h} d\Gamma = 0 \quad (2.21)$$

Introducing approximation of  $\tilde{\boldsymbol{\varepsilon}}^h$  following Eq. (2.18), and performing nodal integration in the variational equation, the discrete equation is obtained:

$$\mathbf{K} \mathbf{u} = \mathbf{f} \quad (2.22)$$

$$\mathbf{K}_{IJ} = \sum_L \tilde{\mathbf{B}}_I^T(\mathbf{x}_L) \mathbf{C} \tilde{\mathbf{B}}_J(\mathbf{x}_L) \quad (2.23)$$

### 2.3 Numerical Test on Stability and Convergence

Stability of SCNI is studied by an eigenvalue analysis of the stiffness matrix of a discretization shown in Fig. 2.2a. With a direct nodal integration without stabilization, 4 zero engenvalues are obtained with the 4-th zero eigenvalue corresponds to a spurious singular mode shown in Fig. 2.2b. Using SCNI, on the other hand, a correct nullity of 3 is obtained, the modes correspond to the 4-th smallest eigenvalue are two deformation modes shown in Fig. 2.2c.

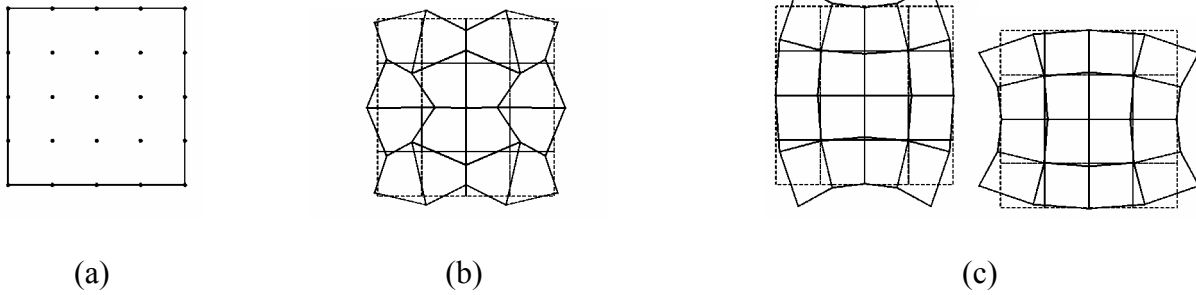


Figure 2.2 Eigenvalue analysis (a) Discrete model, (b) spurious mode in nodal integration, (c) deformation modes corresponding to the -4<sup>th</sup> smallest eigenvalue in SCNI.

A beam problem in Fig. 2.3a is analyzed to study the convergence of SCNI. The  $L_2$  error norm of the direct nodal integration, Gauss integration with  $5 \times 5$  quadrature rule, and the SCNI are compared in Fig. 2.3b, and favorable results of SCNI is shown.

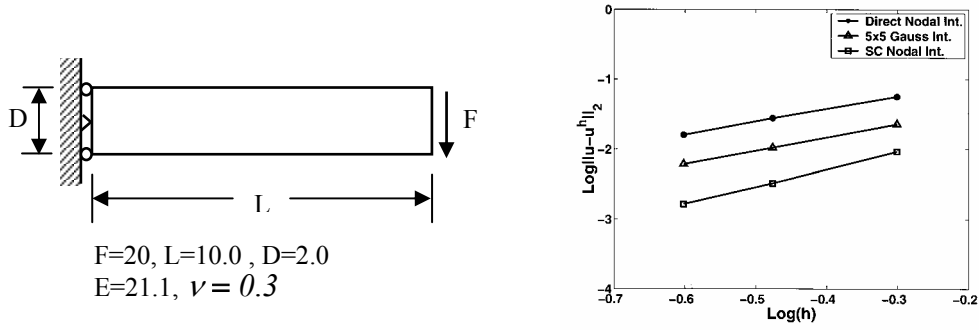


Figure 2.3 Beam problem (a) problem description, (b)  $L_2$  error norms of displacements

### 3. Adaptive Procedures

#### 3.1 Shape function update

Meshfree shape functions are conforming and this offers considerable advantage in adaptivity analysis. In response to the newly added particles, the  $M(\mathbf{x})$  matrix in the shape functions of the existing particles must be reconstructed locally to ensure consistency in the reproducing kernel approximation as follows

$$\begin{aligned}
 M(\mathbf{x}) &= \sum_{I=1}^{NP_{old}} \mathbf{H}(\mathbf{x} - \mathbf{x}_I) \mathbf{H}^T(\mathbf{x} - \mathbf{x}_I) \Phi_a(\mathbf{x} - \mathbf{x}_I) + \sum_{I=1}^{NP_{new}} \mathbf{H}(\mathbf{x} - \mathbf{x}_I) \mathbf{H}^T(\mathbf{x} - \mathbf{x}_I) \Phi_a(\mathbf{x} - \mathbf{x}_I) \\
 &= M_{old}(\mathbf{x}) + \sum_{I=1}^{NP_{new}} \mathbf{H}(\mathbf{x} - \mathbf{x}_I) \mathbf{H}^T(\mathbf{x} - \mathbf{x}_I) \Phi_a(\mathbf{x} - \mathbf{x}_I)
 \end{aligned} \tag{3.1}$$

Note that at  $\mathbf{x}$ , the moment matrix  $M(\mathbf{x})$  changes only when  $\mathbf{x}$  is in a region covered by shape functions of the newly added particles. As shown in Fig.3.2, in addition to the shape functions of the newly added particles, only the shape functions of existing particles with supports intersect with this region need to be updated according to Eq. (3.1). A one-dimensional example with is shown in Fig. 3.2. Inserting a particle between particles 6 and 7 requires reconstruction of shape functions of particles 4, 5, 6, 7, 8, 9 and the new shape function of the new particle 12.

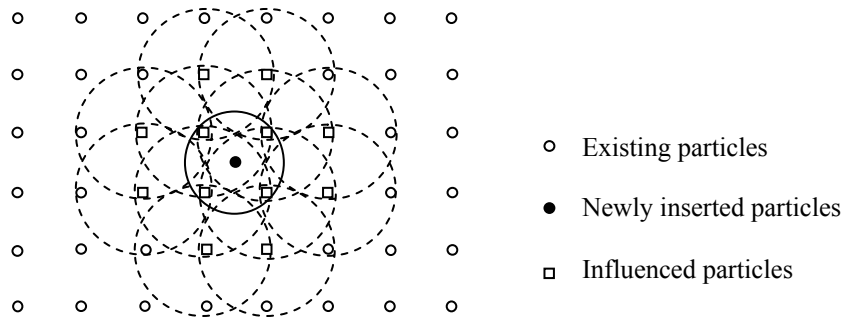
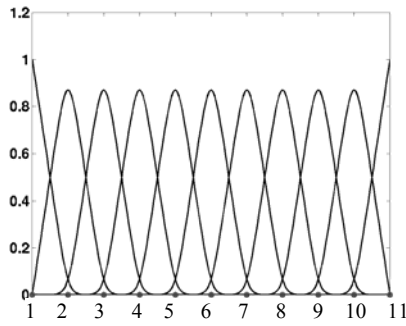
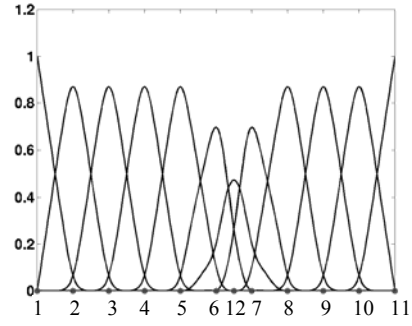


Figure 3.1 Particles influenced by the newly inserted particles in adaptive refinement



(a)



(b)

Figure 3.2 Local reconstruction of shape function: (a) before adaptivity (b) after adaptivity

The topology of Voronoi diagram used in the SCNI discussed in Section 2 is used herein as a reference for inserting particles. Using the properties of Voronoi cell boundary being the perpendicular bisector hyper-plane of a line connecting any two particles, new particles are added at the vertices of the Voronoi cell as shown in Fig. 3.3. Multi-level adaptive refinements for initially uniform and non-uniform particles are shown in Figures 3.4 and 3.5.

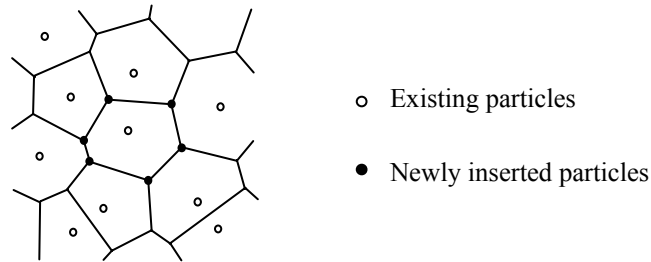


Figure 3.3 Insertion of particles based on Voronoi diagram

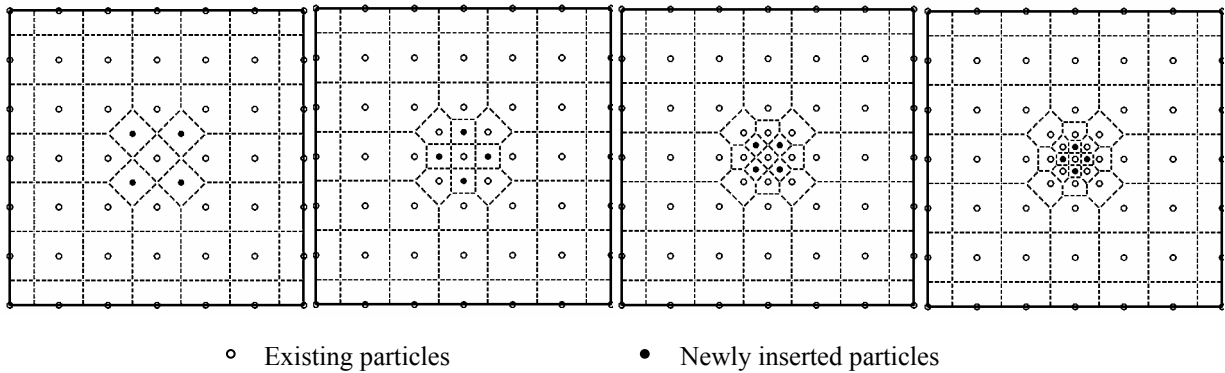


Figure 3.4 Multi-level adaptive refinement on a set of uniformly distributed particles

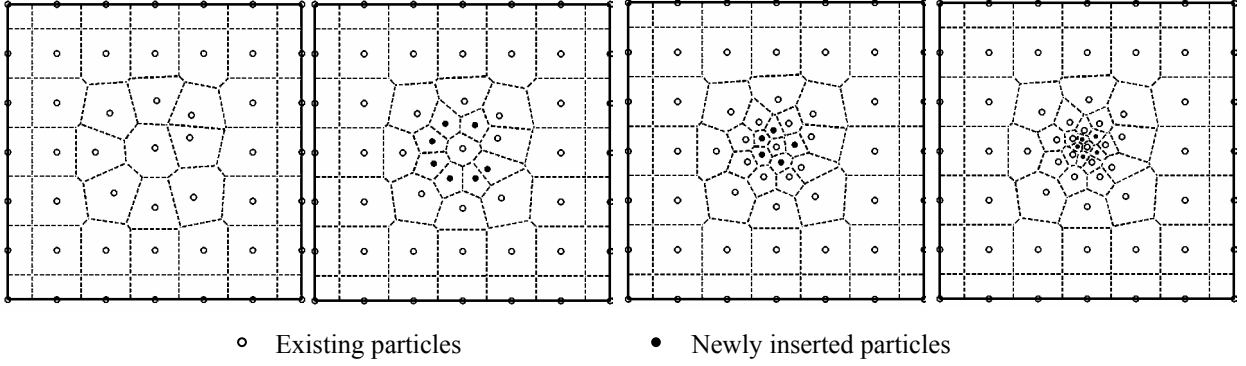


Figure 3.5 Multi-level adaptive refinement on a set of non-uniform distributed particles

In adaptive refinement, the shape function support sizes need to be properly determined. This can be done by using the Voronoi cell information. Denote the Voronoi cell of particle  $P_i$  as  $V(P_i)$ . Using Voronoi diagram, the neighboring particles of particle  $I$  are first identified and grouped as  $B_I$  as shown in Fig. 3.6.

$$B_I = \{P_J : V(P_J) \cap V(P_I) \neq \emptyset\} \quad (3.2)$$

The support size  $a_I$  of particle  $P_I$  is selected as

$$a_I = \alpha_I \cdot \max\{d_J : d_J = \overline{P_I P_J}, \forall P_J \in B_I\} \quad (3.3)$$

In practice,  $\alpha_I$  is chosen between 1.0 and 2.0.

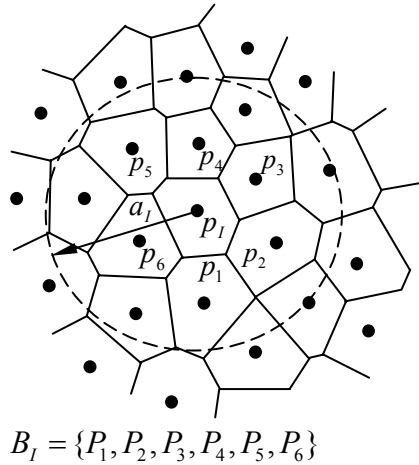


Figure 3.6 Determination of shape function support size

### 3.2 Error indicator

The recovery-based error estimators were first introduced by Zienkiewicz and Zhu [19]. For element Galerkin method, H.J. Chung and T. Belytschko [20] introduced local and global error estimates for the element-free Galerkin (EFG) method. The essence of this error estimate is to use the difference between the values of the recovered stress and those obtained directly by the EFG solution. Since in meshfree method smooth shape functions can be easily constructed, stress recovery can be calculated directly using shape functions as

$$\boldsymbol{\sigma}^*(\mathbf{x}) = \sum_I \Psi_I(\mathbf{x}) \boldsymbol{\sigma}^h(\mathbf{x}_I) = \sum_I \Psi_I(\mathbf{x}) \mathbf{C} \left[ \sum_K \tilde{\mathbf{V}} \Psi_K(\mathbf{x}_I) \mathbf{d}_K \right] \quad (3.4)$$

Equation (3.4) is the reproducing kernel interpolation for stresses. The interpolation error of reproducing kernel interpolation is:

$$\|\boldsymbol{\sigma}^h - \boldsymbol{\sigma}^*\|_{L^2(\Omega)} \leq C_2 a^{m+1} \|\boldsymbol{\sigma}^h\|_{H^{m+1}(\Omega)} \quad (3.5)$$

Since  $\|\boldsymbol{\sigma} - \boldsymbol{\sigma}^h\|_{L^2(\Omega)} \rightarrow 0$  as  $a \rightarrow 0$ , it can be concluded that the recovery solution  $\boldsymbol{\sigma}^*$  will approach the true solution  $\boldsymbol{\sigma}$  in the limit. Thus the error indication of  $\boldsymbol{\sigma}$  is defined as

$$\mathbf{e}_\sigma^* = \boldsymbol{\sigma}^* - \boldsymbol{\sigma}^h \quad (3.6)$$

When the model is sufficiently fine,  $\mathbf{e}_\sigma^*$  approaches true error  $\mathbf{e}_\sigma = \boldsymbol{\sigma} - \boldsymbol{\sigma}^h$ . In meshfree calculation, we define the relative error in energy norm  $\eta^*$  and nodal energy error density  $\rho_I^*$  as follows

$$\eta^* = \frac{\|\mathbf{e}_u^*\|_E}{\|\mathbf{u}^*\|_E} \quad (3.7)$$

$$\|\mathbf{e}_u^*\|_E = \left\{ \frac{1}{2} \sum_{I=1}^I (\boldsymbol{\sigma}^*(\mathbf{x}_I) - \boldsymbol{\sigma}^h(\mathbf{x}_I))^T \mathbf{C}^{-1} (\boldsymbol{\sigma}^*(\mathbf{x}_I) - \boldsymbol{\sigma}^h(\mathbf{x}_I)) A_I \right\}^{1/2} \quad (3.8)$$

$$\|\mathbf{u}^*\|_E = \left\{ \frac{1}{2} \sum_{I=1}^I \boldsymbol{\sigma}^{hT}(\mathbf{x}_I) \mathbf{C}^{-1} \boldsymbol{\sigma}^h(\mathbf{x}_I) A_I \right\}^{1/2} \quad (3.9)$$

$$\rho_I^* = \left( \frac{1}{2} (\boldsymbol{\sigma}^*(\mathbf{x}_I) - \boldsymbol{\sigma}^h(\mathbf{x}_I))^T \mathbf{C}^{-1} (\boldsymbol{\sigma}^*(\mathbf{x}_I) - \boldsymbol{\sigma}^h(\mathbf{x}_I)) \right)^{1/2} \quad (3.10)$$

## 4. Numerical Examples

### 4.1 High-gradient Problem in One Dimension

Consider the following problem

$$\frac{d^2u}{dx^2} + b(x) = 0 \quad \text{in } \Omega \in (0,1) \tag{4.1}$$

$$b(x) = 2s^2 \sec h^2[s(x - 0.5)] \tag{4.2}$$

with boundary conditions given by

$$u(0) = -\tanh(0.5s) \tag{4.3}$$

$$u(1) = \tanh(0.5s) \tag{4.4}$$

Five uniformly refined models with 11, 21, 41, 81, 161 particles (Fig. 4.1a) are used for comparison with the solutions of adaptive models. The meshfree solution is first obtained using 11-particle uniform discretization, and several levels of adaptive refinements are performed based on error indication of each adaptive analysis. The multi-level adaptive refinements are shown in Fig. 4.1b, and the corresponding estimated and true nodal energy error densities for level 2, 3, and 4 are compared in Fig. 4.2. Comparisons of solution  $u$  and  $du/dx$  using different levels of adaptive refinements are given in Figs. 4.3 and 4.4, respectively. The energy error norms of uniform refinement models and adaptive models plotted in Fig. 4.5 show that an adaptive model can achieve the same level of accuracy as that of the uniform refinement model with much fewer particles.

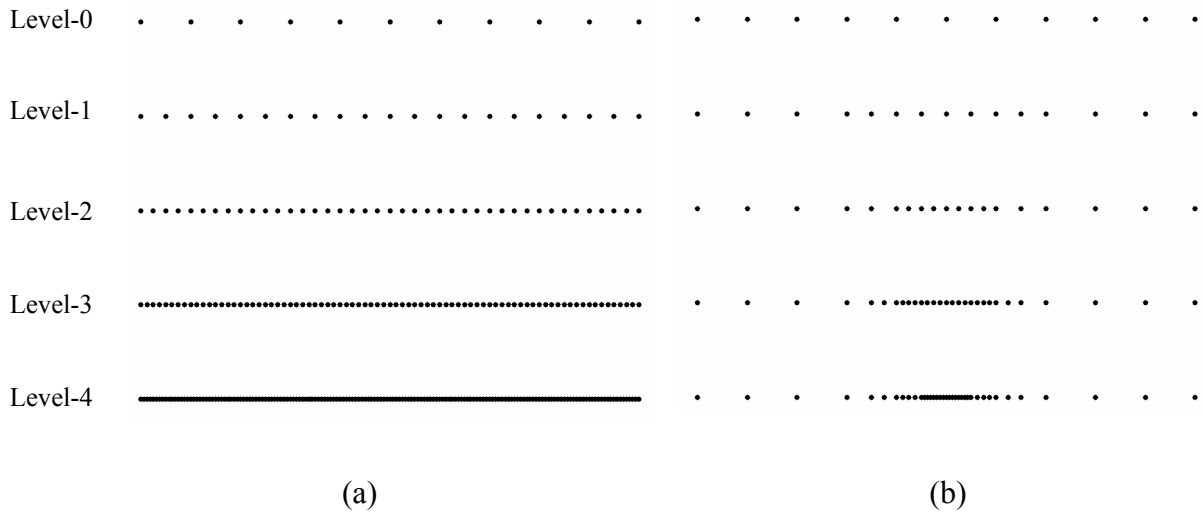


Figure 4.1 (a) Uniform refinements, and (b) adaptive refinements

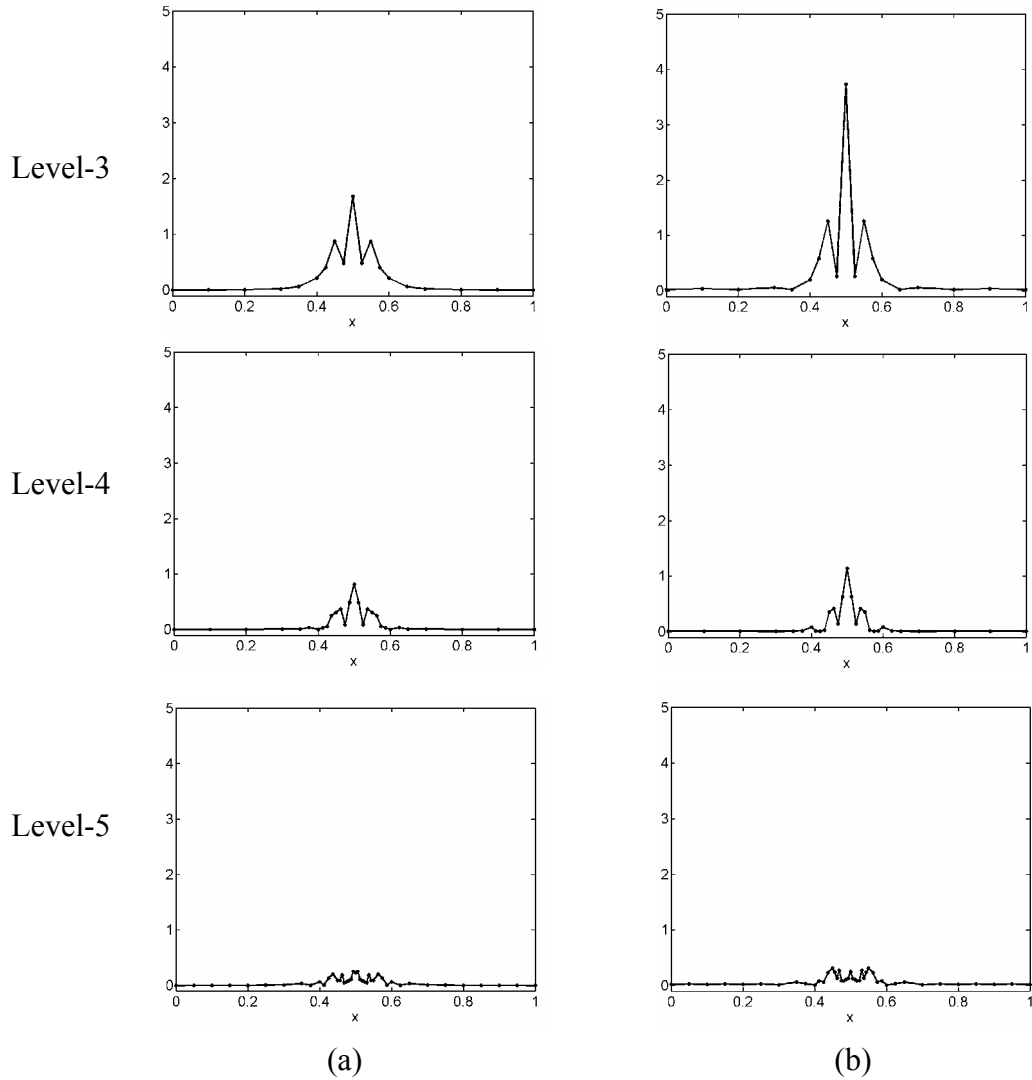


Figure 4.2 Comparison of nodal energy norm (a) error indicator, and (b) true error

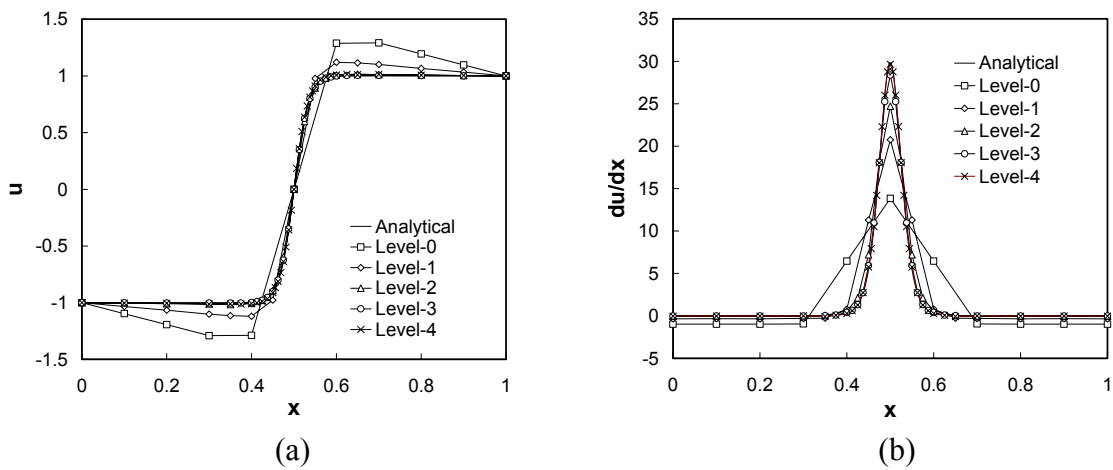


Figure 4.3 Solution of different adaptive refinement models: (a)  $u$ , (b)  $du/dx$

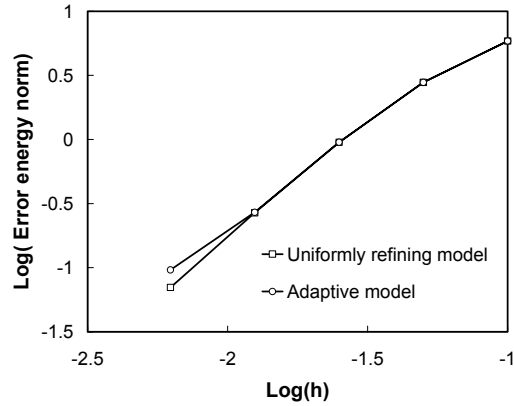


Figure 4.5 Energy error norms of uniformly refined and adaptive models

#### 4.2 Adaptivity of a L-shaped Component

An elastic L-shaped component subjected to a pressure load is shown in Fig. 4.6. Plane stress condition is assumed with the Poisson's ratio of 0.3 and Young's modulus  $E=10^5$ . The energy norm of the solution of a very fine model, considered as an "exact solution", is  $\|\mathbf{u}\|_E^2 = 0.31132$ .

For comparison with solution of adaptive models, uniformly refined models as shown in Fig. 4.7 are generated. Three levels of adaptive refinements based on the energy error density indicator are shown in Fig. 4.8. The error indicator of each adaptive refinement shows large errors near the corner of the L-shaped component. The shear stress distributions of the 833-node uniformly refined model and the 235-node adaptive model are compared in Fig. 4.9, and the results show very good agreement. The energy error norm comparison of the uniformly refined models and the adaptive models in Fig. 4.10 demonstrates the effectiveness of the proposed adaptive Galerkin particle method.

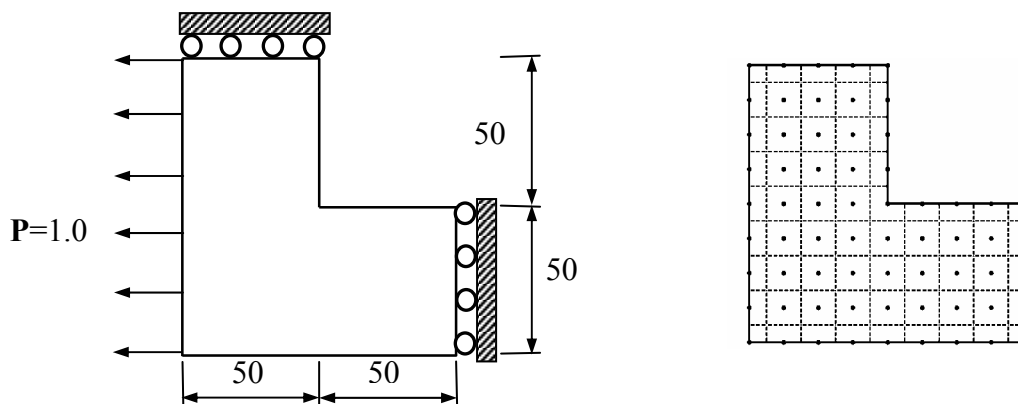
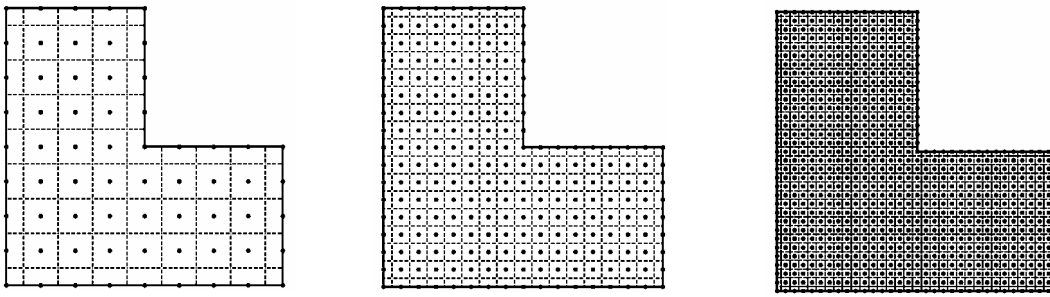


Figure 4.6 L-shape domain in plane stress condition

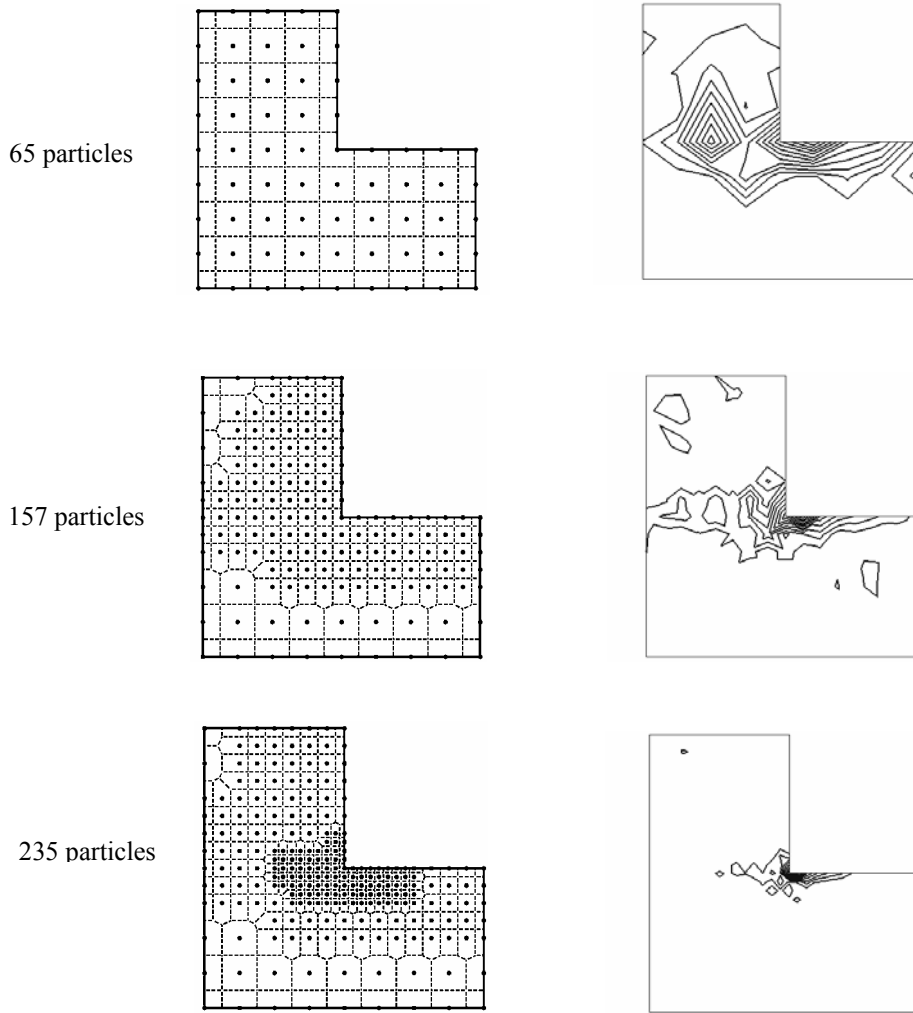


(a) 65 particles

(b) 225 particles

(c) 833 particles

Figure 4.7 Uniformly refined models



65 particles

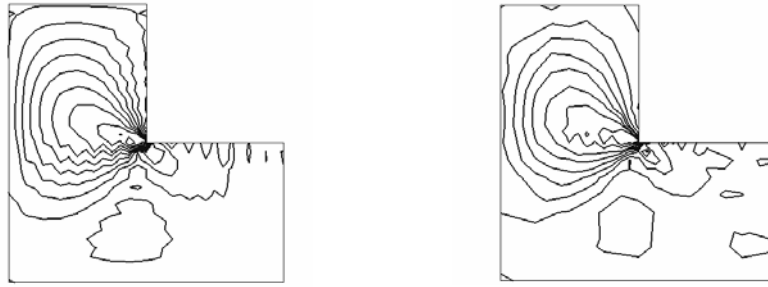
157 particles

235 particles

(a)

(b)

Figure 4.8 (a) Adaptive refinement (b) corresponding energy error density indicator



833 particles uniformly refined model

235 particles adaptive model

Figure 4.9 Comparison of shear stress for uniform and adaptive refinement models

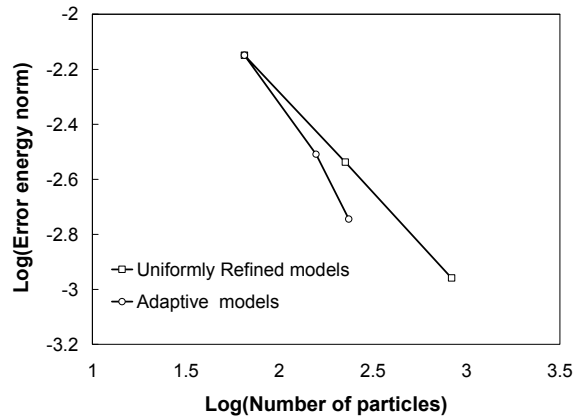


Figure 4.10 Energy error norms of uniform and adaptive refinement models

## 5. Conclusions

Particle based adaptive procedures under the framework of Galerkin particle method has been introduced. The Voronoi diagram used in the stabilized conforming nodal integration in the Galerkin meshfree method provides a basic structure for adaptive refinement. The Voronoi diagram is used for the following purposes: (1) as a geometric reference for particle insertion, (2) for determination of shape function support sizes in the adaptive refinement, (3) obtaining neighboring particle information in data base management.

The conforming and smoothness properties of the reproducing kernel approximation provide substantial advantages in meshfree method over the conventional finite element methods. The error indication based on stress recovery can be implemented effortlessly. This particle based adaptivity approach can be easily extended to large deformation and fracture problems.

## References

1. Monaghan, J. J., "An Introduction to SPH," *Computer Physics Communications*, 48, 89-96 (1988).
2. Nayroles, B., Touzot, G., and Villon, P., "Generalizing the Finite Element Method: Diffuse Approximation and Diffuse Elements," *Computational Mechanics*, 10, 307-318 (1992).
3. Belytschko, T., Lu, Y. Y. and Gu, L., "Element-Free Galerkin Methods," *Int. J. Numer. Meth. Eng.*, 37, 229-256 (1994).
4. Liu, W. K., Jun, S., and Zhang, Y. F., "Reproducing Kernel Particle Methods," *Int. J. Numer. Meth. Fluids.*, 20, 1081-1106 (1995).
5. Chen, J. S., Pan, C., Wu, C. T., and Liu, W. K., "Reproducing Kernel Particle Methods for Large Deformation Analysis of Nonlinear Structures," *Computer Methods in Applied Mechanics and Engineering*, 139, 195-227 (1996).
6. Duarte, C. A. M. and Oden, J. T., "A h-p Adaptive Method Using Clouds," *Comput. Meth. Appl. Mech. Engng.*, 139, 237-262 (1996).
7. Melenk, J. M. and Babuska, I., "The Partition of Unity Finite Element Method: Basic Theory and Applications," *Comput. Meth. Appl. Mech. Engng.*, 139, 289-314 (1996).
8. Sulsky, D., Chen, Z., and Schreyer, H. L., "A Particle Method for History-Independent Materials," *Comput. Meth. Appl. Mech. Engng.*, 118, 179-196 (1994).
9. Atluri, S. N. and Zhu, T., "A new Meshless Local Petrov-Galerkin (MLPG) Approach," *Computational Mechanics*, 22, 117-127 (1998).
10. Sukumar, N., Moran, B., and Belytschko, T., "The Natural Element Method for Solid Mechanics," *Int. J. Numer. Meth. Eng.*, 43, 839-887 (1998).
11. Lancaster, P. and Salkauskas, K. "Surfaces Generated by Moving Least Squares methods," *Mathematics of Computation*, 37, 141-158, (1981).
12. Beissel, S. and Belytschko, T., "Nodal Integration of the Element-Free Galerkin Method," *Comput. Meth. Appl. Mech. Engng.*, 139, 49-74 (1996)
13. Randles, P. W., Libersky, L. D., and Petschek, A. G., "On Neighbors, Derivatives, and Viscosity in Particle Codes," *Proceeding of ECCM conference, Munich, Germany, Aug 31 - Sept 3 (1999)*.
14. Bonet, J. and Kulasegaram, S., "Correction and Stabilization of Smooth Particle Hydrodynamics Methods with Applications in Metal Forming Simulation," *Int. J. Numer. Meth. Eng.* 47, 1189-1214 (1999).
15. Breitkopf, P., Touzot, G., and Villon, P., "Double Grid Diffuse Collocation Method," *accepted, Computational Mechanics (1999)*.
16. Liszka, T. and Orkisz, J., "The Finite Difference Method at Arbitrary Irregular Grids and Its Application in Applied Mechanics," *Computer and Structures*, 11, 83-95 (1980).
17. Chen, J. S., Wu, C. T., Yoon, S., and You, Y., "A Stabilized Conforming Nodal Integration for Galerkin Mesh-free Methods," *Int. J. Numer. Meth. Eng.*, 50, 435-466, (2001).
18. Chen, J. S., Wu, C. T., and Yoon, S. "Nonlinear Version of Stabilized Conforming Nodal Integration for Galerkin Mesh-free Methods," *in press, Int. J. Numer. Meth. Eng.*, (2002).
19. Zienkiewicz, O. C. and Zhu, J. Z., "A Simple Error Estimator and Adaptive Procedure for Practical Engineering Analysis," *Int. J. Numer. Meth. Engng*, 24, 337-357., (1987).
20. Chung, H. J. and Belytschko, T., "An error estimate in the EFG method," *Comput. Mech.* 21, 91-100, (1998).
21. Dolbow, J and Belytschko, T., "Numerical Integration of Galerkin weak Form in Meshfree Methods," *Computational Mechanics*, 23, 219-230 (1999).